

Magnetic field-induced type-II Weyl semimetallic state in geometrically frustrated Shastry-Sutherland lattice GdB_4

Wonhyuk Shon,¹ Dong-Choon Ryu,² Kyoo Kim,^{2,3} B. I. Min,² Bongjae Kim,⁴
Boyoun Kang,⁵ B. K. Cho,⁵ Heon-Jung Kim,^{6,†}, Jong-Soo Rhyee^{1,*}

¹*Department of Applied Physics and Institute of Natural Sciences, Kyung Hee University,
Yongin 17104, Republic of Korea*

²*Department of Physics, Pohang University of Science and Technology, Pohang 37673,
Republic of Korea*

³*Max Plank-POSTECH Korea Research Initiative, Pohang University of Science and
Technology, Pohang 37673, Republic of Korea*

⁴*Department of Physics, Kunsan National University, Gunsan 54150, Korea*

⁵*Department of Materials Science and Engineering, Gwangju Institute of Science and
Technology, Gwangju 61005, Republic of Korea*

⁶*Department of Materials-Energy Science and Engineering, Daegu University, Gyeong-San
38453, Republic of Korea*

Abstract

Weyl semimetal is a topologically non-trivial phase of matter with pairs of Weyl nodes in the k-space, which act as monopole and anti-monopole pairs of Berry curvature. Two hallmarks of the Weyl metallic state are the topological surface state called the Fermi arc and the chiral anomaly. It is known that the chiral anomaly yields anomalous magneto-transport phenomena. In this study, we report the emergence of the type-II Weyl semimetallic state in the geometrically frustrated non-collinear antiferromagnetic Shastry-Sutherland lattice (SSL) GdB_4 crystal. When we apply magnetic fields perpendicular to the non-collinear moments in SSL plane, Weyl nodes are created above and below the Fermi energy along the M-A line (τ -band) because the spin tilting breaks the time-reversal symmetry and lifts band degeneracy while preserving C_{4z} or C_{2z} symmetry. The unique electronic structure of GdB_4 under magnetic fields applied perpendicular to the SSL gives rise to a non-trivial Berry phase, detected in de Haas-van Alphen experiments and chiral-anomaly-induced negative magnetoresistance. The emergence of the magnetic field-induced Weyl state in SSL presents a new guiding principle to develop novel types of Weyl semimetals in frustrated spin systems.

*Email: jsrhyee@khu.ac.kr

†Email: hjkim76@daegu.ac.kr

Keywords: Weyl semimetal, Shastry-Sutherland lattice, GdB_4 , Berry

phase, chiral anomaly.
2019 MSC: 00-01, 99-00

1. Introduction

A Weyl semimetal can be realized by breaking either time-reversal or inversion symmetry in Dirac semimetals. Weyl nodes have opposite chirality with the spin source and spin sink, which can be regarded as a magnetic monopole and anti-monopole, respectively[1]. Weyl nodes are topologically robust against external perturbations[2, 3]. The Weyl semimetallic state has been experimentally observed in mono-pnictides, such as NbP, NbAs, TaP, TaAs[1, 4, 5, 6], and some iridates[7]. These compounds are so-called type-I Weyl semimetals, in which Lorentz symmetry is respected. On the other hand, in type-II Weyl semimetals, the Weyl cones are tilted, breaking the Lorentz symmetry. Because of the tilting of Weyl cones, electron and hole pockets are formed, which is touched at the Weyl nodes[8]. MoTe₂ and WTe₂ are known as type-II Weyl semimetals, driven by broken inversion symmetry[9, 10, 11, 12].

The magneto-transport properties in Dirac and Weyl semimetals such as WTe₂[13], TaP[14], and TaAs[15] include large magnetoresistance with saturating electrical resistivity at low temperatures. Some have argued intimate connection of this phenomenon with nontrivial band topology. However, its origin is still controversial because a huge magnetoresistance can be similarly observed when complete compensation between electrons and holes exists. GdB₄ also shows huge magnetoresistance with saturating electrical resistivity at low temperature[16]. The extremely large magnetoresistance may not be directly related with the non-trivial phase of matter. The more direct manifestation for the nontrivial topology of the Weyl metal is negative longitudinal magnetoresistance originating in Adler-Bell-Jackiw (ABJ) anomalies or chiral anomalies[17, 18, 19, 20, 21]. These phenomenon have been observed in most Dirac and Weyl metals.

RB_4 (R = rare-earth elements) compounds crystallize with a tetragonal structure with a space group of $P4_1/mbm$. The network of magnetic R ions in the $\{001\}$ plane forms a Shastry-Sutherland lattice (SSL) with magnetic coupling among R ions mediated by the Ruderman-Kittel-Kasuya-Yoshida (RKKY) interaction. The SSL is a geometrically frustrated system that consists of a two-dimensional (2D) square lattice with gliding diagonal bonds[22]. According to theoretical studies of the 2D SSL, the breaking of chiral symmetry drives a rich phase diagram containing topological phases with nodal points, such as massless Dirac fermions, quadratic band crossing points, or pseudo-spin 1 Weyl fermions, along with a Mott insulating phase with a large interaction limit[23, 24]. RB_4 (R = rare earth) is one of an archetypal SSL compounds and thus, could exhibit a topological ground state.

Previously, RB_4 has attracted much attention because of its magnetization plateaus, resulting from solidification of the spin-triplet excitation[25, 26]. Among RB_4 compounds, GdB₄ is a system with no magnetization plateaus that possesses a single Néel-type transition below 40 K with a non-collinear magnetic structure. When a compound has topologically non-trivial state such as the Weyl semimetal and Rashba system, there exists a non-zero Berry phase[27, 28, 29]. From the de Haas-van Alphen (dHvA) and Shubnikov-de Haas oscillations

of GdB₄ single crystal, we observed a non-zero Berry phase in the magnetic and electrical transport properties only for $H \parallel [001]$. In addition, we observed chiral anomaly-induced negative longitudinal magnetoresistance (MR). On the other hand, the negative longitudinal MR was absent for the other H directions, which is a strong indication of chiral anomaly-induced magnetoresistance.

From the theoretical investigation based on the density functional theory with a Coulomb interaction (DFT + U), we revealed the emergence of Weyl nodes in GdB₄ when applying a magnetic field $H \parallel [001]$. When H is applied along the $[001]$ direction, the doubly degenerated bands are split due to the breakdown of the time-reversal symmetry T except for the points protected by the C_{4z} or C_{2z} symmetry. The band splitting produces pairs of Weyl nodes near the boundary between electron and hole pockets along the z -direction. As a consequence, a type-II Weyl state, which breaks the Lorentz symmetry is observed. These experimental and theoretical observations constitute clear evidence for a type-II Weyl metallic state in GdB₄ upon the application of a magnetic field, $H \parallel [001]$.

2. Methods

2.1. Theoretical details

We performed first-principles DFT calculations considering the generalized gradient approximation with Coulomb interaction (GGA + U) using the Vienna *ab initio* simulation package (VASP). We applied the Perdew-Becke-Erzenhof (PBE) parameterization for the exchange-correlation functional within the projected augmented wave method with an energy cut off of 600 eV and k-point sampling on a $4 \times 4 \times 4$ grid. The rotationally invariant form of the on-site Coulomb interaction was used with $U_f = 11$ eV and $J_f = 1$ eV for the localized state of the Gd $4f$ states. To simulate the response of the magnetic moment subjected to an external field, we constrained the out of plane component of the Gd moment with an artificial tilting angle. The Gd moment sets up with the tilting angle breaking the original symmetry and accordingly, the double degeneracy of the GdB₄ bands.

2.2. Sample preparation and experimental measurements

GdB₄ single crystals were grown by the Al-flux method. A stoichiometric mixture of Gd (99.9 %) and B (99.9 %) was added to an alumina crucible together with Al (99.999 %) flux at a molar ratio of GdB₄ : Al = 1 : 50. The mixture was melted at 1,500 °C under an argon atmosphere and slowly cooled down to 650 °C with a cooling rate of 5 °C/h. The grown crystals were extracted from the flux by dissolving the Al flux using a NaOH solution. From the X-ray diffraction measurement of the pulverized single crystals, the crystal structure of GdB₄ was identified as a tetragonal symmetry with lattice parameters of $a = 7.136$ Å and $c = 4.038$ Å.

Electrical transport and magnetization measurements were performed using a physical property measurement system (PPMS Dynacool 14 T, Quantum Design, U.S.A) with the VSM option for applying a magnetic field of up to 14 T. A

standard four-contact configuration was employed to measure the temperature-dependent electrical resistivity and magnetoresistance. The de Haas-van Alphen (dHvA) signals were extracted from the plot of magnetization versus magnetic field $M(B)$ by subtracting the background signal.

3. Results and Discussion

Figure 1 presents the inverse magnetic susceptibility $1/\chi(T)$ along the [110] direction and temperature-dependent electrical resistivity $\rho(T)$ for various magnetic fields. An antiferromagnetic transition occurs at $T_N = 43$ K, as presented in Fig. 1a. The effective magnetic moments along the [110] and [001] directions are $7.40 \mu_B$ and $7.37 \mu_B$, respectively, indicating that the magnetic moment comes from the stable Gd^{3+} ions. The spin structure of Gd^{3+} ions below T_N is the isomorphic Archimedean lattice with a Ruderman-Kittel-Kasuya-Yoshida (RKKY) interaction, as presented in the inset of Fig. 1a.

The electrical resistivity $\rho(T)$ exhibits discontinuity of the slope at the transition temperature near $T_N = 43$ K due to the suppression of electron-spin scattering. By applying a magnetic field, $\rho(T)$ below the Néel temperature is significantly increased, showing a saturated value at low temperatures ($T \leq 5$ K), as presented in Fig. 1b. As discussed later, the significant increase of electrical resistivity under applied magnetic fields is due to complete compensation of the electron and hole symmetry in a semimetallic system. The resistivity plateau arises at low temperatures and this may be a signature of additional channels from topologically protected surface states[30].

We performed de Haas-van Alphen (dHvA) oscillation experiments for $H \leq 14$ T, along the [001] direction. Figure 2a shows the dHvA signals as a function of $1/H$ at isothermal temperatures of 2 K, 3 K, and 5 K for applying the magnetic field along the [001] direction. The fast Fourier transformation (FFT) of the dHvA signals shows four main peaks, as shown in Fig. 2b. We denoted the peaks at 8.2 T, 113 T, 126 T, and 176 T as τ , κ , δ , and α , respectively. Using the Onsager relation $A_F = 2\pi^2 F/\Phi_0$ and assuming a circular Fermi surface $A_F = \pi k_F^2$, where F is the frequency and Φ_0 is the magnetic flux quantum, we obtained the cross-sectional area of the Fermi surface A_F and Fermi wave vector k_F , as presented in Table I. The size of A_F for the τ orbit is only $7.8 \times 10^{-4} \text{ \AA}^{-2}$, which is much smaller than the other orbits. The temperature-dependent FFT amplitudes of the dHvA signals decrease with increasing temperature [Fig. 2c]. This behavior is attributed to the temperature damping term in the Lifshitz-Kosevich (LK) formula for the dHvA oscillation, expressed as follows[27, 28, 29].

$$\Delta M = \sum_{i=\alpha,\beta,K} A_i R_T \exp\left(\frac{D_i}{B}\right) \sin\left(2\pi \frac{F_i}{B} + \omega_i\right) \quad (1)$$

here A_i is the amplitude coefficient, ω_i is the phase, and D_i is the Dingle damping factor given by $D_i = -\alpha T_D m^*$, where $\alpha = 2\pi^2 c k_B / e \hbar \approx 14.7$ T/K. T_D is the Dingle temperature $T_D = \hbar / 2\pi k_B \tau_e$, which determines the scattering time τ_e . The subscript i is the band index. R_T is the temperature-dependent FFT

amplitude, given by $R_T = \frac{\alpha m^* T/B}{\sinh(\alpha m^* T/B)}$, where $m^* = m_c/m_e$ is the ratio of the effective cyclotron mass m_c to the free electron mass m_e . The fitting of the FFT amplitudes at different temperatures to the R_T formula yields the effective mass m^* . The m^* values of the τ , κ , δ , and α orbits are 0.07, 0.217, 0.188, and 0.199, respectively. While the effective masses of the κ , δ , and α orbits are of the order ~ 0.2 , the mass of the τ orbit is considerably small. The observations that both the Fermi surface area and effective mass approach zero are characteristics of the doped Dirac or Weyl band where E_F is located very near the nodal point. Therefore, the small cross-sectional area of the Fermi surface in the τ band with a small effective mass may represent the existence of a Weyl or Dirac band. Indeed, these characteristics were observed in the Weyl semimetal TaP[29].

Since F and m^* have been determined, the oscillating components of the dHvA signals can be fitted directly to the LK formula to obtain the Dingle temperature T_D and phase factor ω_i , where we considered four orbits of τ , κ , δ , and α . The fitting of the dHvA signal at 3 K (black line) to the LK formula (red line) shows relatively good correspondence with the $2\pi\Gamma$ non-zero Berry's phase [upper panel of Fig. 2d compared without consideration of $2\pi\Gamma$. The values of T_D and ω_i along with other parameters are summarized in Table I. The Dingle temperature of the τ -orbit ($T_D = 0.49$ K) is lower than those of the other bands (3.05-7.24 K) by one order of magnitude. From the relations of $T_D = \hbar/2\pi k_B \tau_e$ and $\mu = e\tau_e/m^*$, where μ is the mobility and the Dingle temperature $T_D = 0.49$ K, the relaxation time and mobility of the τ -orbit were determined to be $\tau_e = 2.48 \times 10^{-12}$ s and $\mu = 5.7 \times 10^4$ cm² V⁻¹ s⁻¹, respectively. The μ value of the τ -orbit is significantly larger than those of the other orbits. When E_F is very close to the node, the impurity scattering is drastically reduced, as previously observed in graphene[31] and BiTeI[32]. Thus, the large value of μ implies Dirac or Weyl metallicity of the orbit.

Another important observation is the non-trivial phase factor for the τ -orbit, ω_τ . The phase factor in Eq. (1) is expressed as $\omega_i = -2\pi(1/2 - \Gamma_i + \Delta_i)$, where $2\pi\Gamma_i$ is the Berry's phase and Δ_i is the phase shift arising from the shape and dimensionality of the Fermi surface for the i th-orbit. For instance, $\Delta = \pm 1/8$ for the three-dimensional Fermi surface and $\Delta = 0$ for the two-dimensional case. As summarized in Table I, the Berry phase of the τ -band is $2\pi\Gamma_\tau = (1.33 \pm 0.25)\pi$. The non-zero Berry phase is non-trivial and it indicates the existence of Dirac relativistic fermions[33]. Therefore, this non-trivial value of the Berry phase suggests non-zero Berry's curvature of the relativistic Dirac fermions.

To understand the origin of the non-zero Berry phase, we performed the *ab initio* first principle calculations of the GdB₄ compound using DFT+U. To clarify the spin configuration in GdB₄[34], we calculated dHvA frequencies assuming three different magnetic structures to compare to the experiments: the non-collinear magnetic structure (NCM), an antiferromagnetic state with an easy axis along the z -direction (AFM1), and a ferromagnetic structure with spins fully polarized along the $+z$ direction (FM). The experimental frequencies of τ , κ , δ , and α were well reproduced by the DFT calculations based on the NCM structure. Among the three different spin structures, the dHvA fre-

quencies, calculated from the NCM case, are consistent with the experimentally measured dHvA frequencies (not shown here), indicating that the NCM structure is the ground state spin configuration in GdB₄, as presented in the inset of Fig. 1a.

The NCM structure has 8 symmetry operations: E , C_{4z} , C_{2z} , C_{-4z} , R_0C_{2y} , $R_0C_{2(x+y)}$, R_0C_{2x} , and $R_0C_{2(x-y)}$, where R_0 is the translation operator $R([1/2, 1/2, 0])$. Also, the system is invariant under the $T \otimes I$ operation, where T and I are the time-reversal and inversion operators, respectively. Note that the TI symmetry guarantees Kramer's degeneracy over the whole Brillouin zone in the NCM configuration and all bands are degenerated as shown in Fig. 3a.

When we apply a magnetic field along the $[001]$ direction, the non-symmorphic operations are not invariant anymore because non-collinear spins are tilted along the magnetic field direction and break the time-reversal symmetry. Moreover, the finite magnetic moments induced by the tilting of spins break the $T \otimes I$ invariance of the system. To simulate the band structure under an external magnetic field, we artificially tilted the moment by 10, 20, and 90 degrees. In all of the situations, accidental crossings of the topological bands occur along the Γ -Z and A-M lines. Assuming a non-extreme external magnetic field, hereafter, we consider the 10 degree case. The DFT calculation with the artificial spin tilt suggests the possibility of Weyl points connected to the α , δ , and τ orbits. Therefore, the double degeneracy of bands in the NCM structure lifts except for points which are protected by C_{4z} or C_{2z} operation along the Γ -Z and M-A paths, as shown in Fig. 3b. When we expand the band crossing regions marked in the green circle and red rectangle along the A-M and Γ -Z lines in Fig. 3b, multiple band crossing points appear, as shown in Figs. 3c and 3d, respectively.

For the three different band crossing points denoted by WP1, WP2, and WP3, we applied the Wilson loop analysis. Figure 3e presents the flows of the Wannier charge center along the two different poles (south and north) at the WP1, WP2, and WP3 points, respectively. The existence of spin chirality, as confirmed by the Wannier charge flow, indicates the topologically non-trivial character of Weyl points along the Γ -Z and M-A paths. Both the symmetry and Wilson loop analysis identifies 3 pairs of Weyl nodes along the lines with opposite chiral charges, which are protected by the C_{4z} or C_{2z} symmetry. The separation of Weyl nodes depends on the strength of the magnetic field. As the magnetic field is progressively applied, WP1 is shifted toward the conduction band while WP2 and WP3 are shifted toward the valence band on the order of $g\mu_B B$, where g is the Landé g -factor.

Figures 4a~d present four Fermi surfaces of an GdB₄ in the absence of external magnetic field. The extremal orbits for $H \parallel [001]$ are depicted on each Fermi surface[35]. We identified the orbits by α , δ , and τ bands, which correspond to the experimentally identified orbits from the dHvA oscillation. Note that the Weyl points exist along the Γ -Z line, as presented in Fig. 4g. We performed the Berry curvature calculation in the M-A ($k_z = 0$) and Γ -Z ($k_z = \pi$) planes. It is noteworthy that there are finite integrated values of Berry curvature around the M and Z points, as presented in Figs. 4e and f, respectively. The finite Berry curvatures near the M and Z points correspond to the non-zero Berry phase at

the τ , δ , and α orbits. Therefore, the non-zero Berry phases of the orbits are caused by the Weyl nodes, as clearly evidenced by the Wannier charge flow at the Weyl nodes.

Because the Berry curvatures by the Weyl nodes are identified in the Fermi surface, we can expect that the unconventional magneto-transport is associated with the chiral current. In the Weyl semimetal, the pair of Weyl nodes serves as a chiral charge as a sink and source within the Berry curvature. When we apply a magnetic field parallel to the electric field direction $H \parallel E$, the Weyl nodes result in a dissipationless conduction channel, which is known as a chiral anomaly. In a Dirac semimetal with doubly degenerated linear band dispersion, the external H splits a single Dirac cone into a pair of Weyl cones with different chiralities along the direction of H . The separation of Weyl nodes increases the current flow, resulting in a decrease of electrical resistivity (i.e., an increase of electrical conductivity)[18]. This negative longitudinal magnetoresistance (MR) has been observed in several Dirac and Weyl semimetals, such as $\text{Bi}_{0.96}\text{Sb}_{0.04}$ [19], Na_3Bi [36], Cd_3As_2 [37], TaP [38], TaAs [1], and GdPtBi [15, 39]. The chiral anomaly also induces a difference of the Fermi level E_F between the paired Weyl bands when inter-node scatterings are negligible. This phenomenon, known as charge pumping, was recently demonstrated as nonlinear electrical conductivity, which is proportional to the square of the electric field E^2 [40].

Compared to a typical Dirac semimetal with a doubly degenerated linear dispersion, GdB_4 is different in that the type-II Weyl semimetallic state is manifested near the Fermi level, which is due to a crossing of spin-splitting valence and conduction bands solely for $H \parallel [001]$. This also gives rise to a chiral-anomaly-induced negative MR depending on the H -field direction. Figure 5a shows the longitudinal magnetoconductivity (MC, the inverse of MR) as a function of the magnetic field H for the $[001]$ direction at several temperatures below 6 K. The peak in the low magnetic field region is due to the weak antilocalization effect, which has been observed in other Dirac and Weyl semimetals[41, 42]. For the high magnetic field region ($H \geq 2$ T), a positive MC (negative MR) is observed. For a more quantitative analysis, we used the conductivity formula derived from the Boltzmann transport equation[19]. This formula considers charge transport contributions from both the Weyl and normal bands, along with the weak antilocalization (WAL) effect. In the weak field limit, the longitudinal magneto-conductivity $\sigma_L(H)$ is expressed by $\sigma_L(H) = (1 + C_W H^2)\sigma_{WAL} + \sigma_n$, where σ_{WAL} and σ_n are the conductivities of the WAL corrections and normal bands, respectively, and C_W is the coefficient of conductivity enhancement resulting from chiral anomaly. The fitting results, as represented by the solid lines in Fig. 5a show that the theoretical fittings reproduce the experimental results. From the fitting of the relationship, the value of C_W was found to increase with decreasing temperature and suddenly approached zero at around 6 K as presented in Fig. 5b.

Figure 5c compares the magnetoconductivities for different magnetic field directions of $H \parallel [001]$ (black square) and $H \parallel [110]$ (red circle). While the electrical conductivity σ_{xx} for $H \parallel [001]$ shows a positive slope at the high magnetic

field beyond the weak antilocalization region, σ_{xx} is negative for the $H \parallel [110]$ overall magnetic field range. This is remarkable because this type of disparity in electrical transport for magnetic field directions has never been observed in other Dirac and Weyl semimetals. The disparity of the magnetoconductivity behavior is attributed to the unique band structure of GdB₄, which is associated with the spin configuration in SSL.

When we apply a magnetic field along the $H \parallel [110]$ direction, the DFT + U calculations confirmed the absence of Weyl nodes near the Fermi level E_F . In contrast, for $H \parallel [001]$ along the Z-line, E_F resides in between the Weyl nodes at a different energy. In this condition, the Weyl nodes contribute to the magneto-transport because of the existence of a chiral current (source and sink of chiral charges), resulting in the positive MC (negative MR). This is consistent with the enhancement of the chiral current contribution at temperatures below $T \leq 6$ K for $H \parallel [001]$, as presented in Fig. 5b. The antiferromagnetic SSL and its spin canting along the $H \parallel [001]$ direction lift the band degeneracy while preserving the Kramers degeneracy at some points due to protecting C_{4z} or C_{2z} symmetry, giving rise to the emergence of Weyl nodes at low temperatures.

Another important implication of MC, as shown in Fig. 5c, is the complete exclusion of the current jetting effect, which is readily caused by the non-uniform current distribution inside the sample. The non-homogeneous current injection can cause negative MR[43]. As the sample dimensions in the two cases for $H \parallel [001]$ and $H \parallel [110]$ are identical, there should be positive MC in both cases if we assume that the current jetting effect. Therefore, we can exclude the possibility of an extrinsic effect on the negative MR due to an inhomogeneous current distribution. The angle-dependent MR shows negative magneto-resistance only when the magnetic field direction is parallel to the electric current direction, $H \parallel I$ ($\theta \approx 90^\circ$, where θ is the angle between H and the normal direction of the sample), as presented in Fig. 5d. With increasing deviation angle between the magnetic field direction and the electrical current direction ($\theta \leq 88^\circ$), the negative MR evolves to positive MR behavior.

Finally, we evaluated the relationship between the extreme MR and Weyl semimetallic property. As mentioned before, the extreme MR has been considered as a possible signature of the Weyl semimetallic state in several reports[44, 45, 30]. We also observed an extremely large MR at low temperatures in GdB₄, as presented in Fig. 1b. Another origin for the extreme MR is the complete compensation of electrons and holes in semimetals. To validate the compensation scenario, we employed multiple-carrier models in the simultaneous analysis of electrical resistivity and Hall resistivity. With the existence of multiple charge carriers, the total conductivity is given as follows:

$$\sigma(H) = e \left[\sum_{e=1}^n \frac{n_e \mu_e}{1 + i \mu_e H} + \sum_{h=1}^{n'} \frac{n_h \mu_h}{1 + i \mu_h H} \right] \quad (2)$$

where $n_{e(h)}$ and $\mu_{e(h)}$ are the carrier density and Hall mobility of electrons (holes), respectively, and $n(n')$ is the number of electrons (holes) channel.

The real and imaginary parts of equation (2) are the longitudinal conductivity $\sigma_{xx}(H)$ and Hall conductivity $\sigma_{xy}(H)$, respectively. The longitudinal and Hall conductivities are transformed to resistivity and Hall resistivity using the formulas $\rho(H) = \sigma_{xx}/(\sigma_{xx}^2 + \sigma_{xy}^2)$ and $\rho_H(H) = \sigma_{xy}/(\sigma_{xx}^2 + \sigma_{xy}^2)$.

Figures 6a and 6b show the longitudinal electrical resistivity ρ_{xx} and Hall resistivity ρ_{xy} with theoretical fitting (color lines) using the three-carrier model. Here, we assumed the existence of two-electron and one-hole carriers because the κ , τ , and δ orbits correspond to the bands. The three-carrier model describes the experimental data quite well. Based on the analysis of $\rho(H)$ and $\rho_H(H)$, the values of n and μ were obtained for the three carriers, as presented in Table II. The density of second electron carriers (n_{e2}) is smaller by three orders of magnitude than the other carriers at low temperatures. This observation is also very consistent with the density of the τ orbit calculated from the frequency of the dHvA oscillation, which is smaller than those of the other orbits by two orders of magnitude. Thus, the orbit likely corresponds to the electron carrier with a small carrier density.

Note that there is almost complete compensation of electrons and holes: $n_e + n_e^\tau \approx n_h$, where n_e^τ is the electronic density of the τ orbit. Moreover, Fig. 6c demonstrates the reproduction of $\rho(T)$ at different magnetic fields, using the parameter values estimated by the analysis of $\rho(H)$ and $\rho_H(H)$. This behavior of magnetotransport is commonly observed for both cases of $H \parallel [001]$ and $H \parallel [110]$. This strongly suggests that the compensation of electron and hole carriers is the origin of the extreme MR in GdB₄.

4. Conclusions

In summary, we observed the emergence of the magnetic field induced type-II Weyl semimetallic state in GdB₄. When we applied the magnetic field along the $H \parallel [001]$ direction, the in-plane non-collinear Shastry-Sutherland lattice-type antiferromagnetic spins tilted to the magnetic field direction. The breaking of time-reversal symmetry by spin tilting lifts the band degeneracy. At some points, the C_{4z} or C_{2z} symmetry is conserved so that band degeneracies exist along the Γ -Z and M-A paths. We found that the Kramers degeneracy points are confirmed as Weyl points from the Wilson loop analysis. The theoretical investigation of the Fermi surface and Berry's phase on GdB₄ is consistent with the experimental results obtained from the dHvA analysis. The DFT calculations within artificial spin tilting suggest the possibility of a Weyl point connected to the α , δ , and τ orbits. The non-zero Berry phase and chiral current in the dHvA and magneto-transport behavior supports the Weyl semimetallic property for applying the magnetic field along the $H \parallel [001]$ direction. The electron-hole compensation effect confirms the colossal MR in the GdB₄ from the multiple carrier model of the anisotropic magneto-transport measurements. This research suggests a new principle for the emergence of the Weyl semimetallic state in the SSL system. Also, it shows that the Weyl semimetallic state can be controlled by external magnetic field, so we can investigate the topological phase transition in terms of magnetic field strength.

5. acknowledgments

J.S.R. was supported by a grant from Kyung Hee University (20171203).
H.J.K. was supported by a grant from the NRF (Grant No. 2017R1A2B2002731).
D.C.R. and B.I.M. acknowledge support from the NRF (Grant No. 2017R1A2B4005175).
K.K. was supported by grants from the NRF (Grant No. 2016R1D1A1B02008461)
and Max-Planck POSTECH/KOREA Research Initiative (Grant No. 2016K1A4A4A01922028).
B.J.K. was supported by a grant from the NRF (Grand No. 2018R1D1A1A02086051).

References

- [1] S.-Y. Xu, I. Belopolski, N. Alidoust, M. Neupane, G. Bian, C. Zhang, R. Sankar, G. Chang, Z. Yuan, C.-C. Lee, S.-M. Huang, H. Zheng, J. Ma, D. S. Sanchez, B. Wang, A. Bansil, F. Chou, P. P. Shibayev, H. Lin, S. Jia, M. Z. Hasan, Discovery of a Weyl fermion semimetal and topological Fermi arcs, *Science* 349 (2015) 613.
- [2] S. Murakami, Phase Transition between the Quantum Spin Hall and Insulator Phases in 3D: Emergence of a Topological Gapless Phase, *New J. Phys.* 9 (2007) 356.
- [3] S. Murakami, Gap Closing and Universal Phase Diagrams in Topological Insulators, *Physica E* 43 (2011) 748.
- [4] B. Q. Lv, H. M. Weng, B. B. Fu, X. P. Wang, H. Miao, J. Ma, P. Richard, X. C. Huang, L. X. Zhao, G. F. Chen, Z. Fang, X. Dai, T. Qian, H. Ding, Experimental Discovery of Weyl Semimetal TaAs, *Phys. Rev. X* 5 (2015) 031013.
- [5] S.-M. Huang, S.-Y. Xu, I. Belopolski, C.-C. Lee, G. Chang, B. Wang, N. Alidoust, G. Bian, M. Neupane, C. Zhang, S. Jia, A. Bansil, H. Lin, M. Z. Hasan, Weyl Fermion semimetal with surface Fermi arcs in the transition metal monpnictide TaAs class, *Nat. Commun.* 6 (2015) 7373.
- [6] J. Gooth, A. C. Niemann, T. Meng, A. G. Grushin, K. Landsteiner, B. Gotsmann, F. Menges, M. Schmidt, C. Shekhar, V. Süß, R. Hühne, B. Rellinghaus, C. Felser, B. Yan, and K. Nielsch, Experimental signatures of the mixed axial-gravitational anomaly in the Weyl semimetal NbP, *Nature* 547 (2017) 324.
- [7] X. Wan, A. M. Turner, A. Vishwanath, S. Y. Savrasov, Topological Semimetal and Fermi-Arc Surface States in the Electronic Structure of Pyrochlore Iridates, *Phys. Rev. B* 83 (2011) 205101.
- [8] A. A. Soluyanov, D. Gresch, Z. Wang, Q. S. Wu, M. Troyer, X. Dai, B. A. Bernevig, Type-II Weyl semimetals, *Nature* 527 (2015) 495.
- [9] K. Deng *et al.*, Experimental observation of topological Fermi arcs in type-II Weyl semimetal MoTe₂, *Nat. Phys.* 12 (2016) 1105.
- [10] K. Zhang, C. Bao, Q. Gu, X. Ren, H. Zhang, K. Deng, Y. Wu, Y. Li, J. Feng, S. Zhou, Raman signatures of inversion symmetry breaking and structural phase transition in type-II Weyl semimetal MoTe₂, *Nat. Commun.* 7 (2016) 13552.
- [11] Z. Wang, D. Gresch, A. A. Soluyanov, W. Xie, S. Kushwaha, X. Dai, M. Troyer, R. J. Cava, B. A. Bernevig, MoTe₂: A Type-II Weyl Topological Metal, *Phys. Rev. Lett.* 117 (2016) 056805.

- [12] G. Autès, D. Gresch, M. Troyer, A. A. Soluyanov, O. V. Yazyev, Phys. Rev. Lett. 117 (2016) 066402.
- [13] M. N. Ali, J. Xiong, S. Flynn, J. Tao, Q. D. Gibson, L. M. Schoop, T. Liang, N. Haldolaarachchige, M. Hirschberger, N. P. Ong, R. J. Cava, Large, non-saturating magnetoresistance in WTe₂, Nature 514 (2014) 205.
- [14] C. Zhang, C. Guo, H. Lu, X. Zhang, Z. Yuan, Z. Lin, J. Wang, and S. Jia, Large magnetoresistance over an extended temperature regime in monophosphides of tantalum and niobium, Phys. Rev. B 92 (2015) 041203(R).
- [15] X. Huang, L. Zhao, Y. Long, P. Wang, D. Chen, Z. Yang, H. Liang, M. Xue, H. Weng, Z. Fang, X. Dai, G. Chen, Observation of the Chiral-Anomaly-Induced Negative Magnetoresistance in 3D Weyl Semimetal TaAs, Phys. Rev. X 5 (2015) 031023.
- [16] B. K. Cho, J.-S. Rhyee, J. Y. Kim, M. Emilia, P. C. Canfield, Anomalous magnetoresistance at low temperatures ($T \leq 10$ K) in a single crystal of GdB₄, J. Appl. Phys. 97 (2005) 10A923.
- [17] H. B. Nielsen, M. Ninomiya, The Adler-Bell-Jackiw anomaly and Weyl fermions in a crystal, Phys. Lett. B 130 (1993) 389.
- [18] D. T. Son, B. Z. Spivak, Chiral anomaly and classical negative magnetoresistance of Weyl metals, Phys. Rev. B 88 (2013) 104412.
- [19] H.-J. Kim, K.-S. Kim, J.-F. Wang, M. Sasaki, N. Satoh, A. Ohnishi, M. Kitaura, M. Yang, L. Li, Dirac versus Weyl Fermions in Topological Insulators: Adler-Bell-Jackiw Anomaly in Transport Phenomena, Phys. Rev. Lett. 111 (2013) 246603.
- [20] Y.-Y. Lv, X. Li, B.-B. Zhang, W. Y. Deng, S.-H. Yao, Y. B. Chen, J. Zhou, S.-T. Zhang, M.-H. Lu, L. Zhang, M. Tian, L. Sheng, Y.-F. Chen, Experimental Observation of Anisotropic Adler-Bell-Jackiw Anomaly in Type-II Weyl Semimetal WTe_{1.98} Crystals at the Quasiclassical Regime, Phys. Rev. Lett. 118 (2017) 096603.
- [21] Y. Wang *et al.*, Gate-tunable negative longitudinal magnetoresistance in the predicted type-II Weyl semimetal WTe₂, Nat. Commun. 7 (2016) 13142.
- [22] B. S. Shastry, B. Sutherland, Exact ground state of a quantum mechanical antiferromagnet, Physica B 108 (1981) 1069.
- [23] T. Kariyado, Y. Hatsugai, Symmetry-protected quantization and bulk-edge correspondence of massless Dirac fermions: Application to the fermionic Shastry-Sutherland model, Phys. Rev. B 88 (2013) 245126.
- [24] H.-D. Liu, Y.-H. Chen, H.-F. Lin, H.-S. Tao, W.-M. Liu, Antiferromagnetic Metal and Mott Transition on Shastry-Sutherland Lattice, Sci. Rep. 4 (2014) 4829.

- [25] S. Yoshii, T. Yamamoto, M. Hagiwara, S. Michimura, A. Shigekawa, F. Iga, T. Takabatake, K. Kindo, Multistep Magnetization Plateaus in the Shastry-Sutherland System TbB_4 , *Phys. Rev. Lett.* 101 (2008) 087202.
- [26] P. A. McClarty, F. Krüger, T. Guidi, S. F. Parker, K. Refson, A. W. Parker, D. Prabhakaran, R. Coldea, Topological triplon modes and bound states in a Shastry-Sutherland magnet, *Nat. Phys.* 13 (2017) 736.
- [27] H. Murakawa, M. S. Bahramy, M. Tokunaga, Y. Kohama, C. Bell, Y. Kaneko, N. Nagaosa, H. Y. Hwang, Y. Tokura, Detection of Berry's phase in a bulk Rashba semiconductor, *Science* 342 (2013) 1490.
- [28] P. Sergelius, J. Gooth, S. Babler, R. Zierold, C. Wiegand, A. Niemann, H. Reith, C. Shekhar, C. Felser, B. Yan, K. Nielsch, Berry phase and band structure analysis of the Weyl semimetal NbP, *Sci. Rep.* 6 (2016) 33859.
- [29] J. Hu, J. Y. Liu, D. Graf, S. M. A. Radmanesh, D. J. Adams, A. Chuang, Y. Wang, I. Chiorescu, J. Wei, L. Spinu, Z. Q. Mao, π Berry phase and Zeeman splitting of Weyl semimetal TaP, *Sci. Rep.* 6 (2016) 18764.
- [30] F. F. Tafti, Q. D. Gibson, S. K. Kushwaha, N. Haldolaarachchige, R. J. Cava, Resistivity plateau and extreme magnetoresistance in LaSb, *Nat. Phys.* 12 (2015) 272.
- [31] Y. Zhang, Y.-W. Tan, H. L. Stormer, P. Kim, Experimental observation of the quantum Hall effect and Berry's phase in graphene, *Nature* 438 (2005) 201.
- [32] M. Sasaki, K.-M. Kim, A. Ohnishi, M. Kitaura, N. Tomita, V. A. Kurbachinskii, K.-S. Kim, H.-J. Kim, Interplay between disorder and inversion symmetry: Extreme enhancement of the mobility near the Weyl point in BiTeI, *Phys. Rev. B* 92 (2015) 205121.
- [33] W. Desrat, C. Consejo, F. Tepe, S. Contreras, M. Marcinkiewicz, W. Knap, A. Nateprov, E. Arushanov, Non-trivial Berry phase in the Cd_3As_2 3D Dirac semimetal, *J. Phys. Conf. Series* 647 (2015) 012064.
- [34] M. N. Huda, L. Kleinman, DFT+U search for the energy minimum among eight collinear and noncollinear magnetic structures of GdB_4 , *Phys. Rev. B* 78 (2008) 094424.
- [35] P.M.C. Rourke, S.R. Julian, Numerical extraction of de Haas-van Alphen frequencies from calculated band energies, *Comp. Phys. Commun.* 183 (2012) 324.
- [36] J. Xiong, S. K. Kushwaha, T. Liang, J. W. Krizan, M. Hirschberger, W. Wang, R. J. Cava, N. P. Ong, Evidence for the chiral anomaly in the Dirac semimetal Na_3Bi , *Science* 350 (2015) 413.

- [37] P. J. W. Moll, N. L. Nair, T. Helm, A. C. Potter, I. Kimchi, A. Vishwanath, J. G. Analytis, Transport evidence for Fermi-arc-mediated chirality transfer in the Dirac semimetal Cd_3As_2 , *Nature* 535 (2016) 266.
- [38] Z. K. Liu, L. X. Yang, Y. Sun, T. Zhang, H. Peng, H. F. Yang, C. Chen, Y. Zhang, Y. F. Guo, D. Prabhakaran, M. Schmidt, Z. Hussain, S.-K. Mo, C. Felser, B. Yan, Y. L. Chen, Evolution of the Fermi surface of Weyl semimetals in the transition metal pnictide family, *Nat. Mater.* 15 (2016) 27.
- [39] M. Hirschberger, S. Kushwaha, Z. Wang, Q. Gibson, S. Liang, C. A. Belvin, B. A. Bernevig, R. J. Cava, N. P. Ong, The chiral anomaly and thermopower of Weyl fermions in the half-Heusler GdPtBi , *Nat. Mater.* 15 (2016) 1161.
- [40] D. Shin, Y. Lee, M. Sasaki, Y. H. Jeong, F. Weickert, J. B. Betts, H.-J. Kim, K.-S. Kim, J. Kim, Violation of Ohm's law in a Weyl metal, *Nat. Mater.* 16 (2017) 1096.
- [41] B. Fu, H.-W. Wang, S.-Q. Shen, Quantum Interference Theory of Magnetoresistance in Dirac Materials, *Phys. Rev. Lett.* 122 (2019) 246601.
- [42] S. Liang, J. Lin, S. Kushwaha, J. Xing, N. Ni, R. J. Cava, N. P. Ong, Experimental Tests of the Chiral Anomaly Magnetoresistance in the Dirac-Weyl Semimetals Na_3Bi and GdPtBi , *Phys. Rev. X* 8 (2018) 031002.
- [43] R. D. dos Reis, M. O. Ajeesh, N. Kumar, F. Arnold, C. Shekhar, M. Naumann, M. Schmidt, M. Nicklas, E. Hassinger, On the search for the chiral anomaly in Weyl semimetals: the negative longitudinal magnetoresistance, *New J. Phys.* 18 (2016) 085006.
- [44] F. C. Chen, H. Y. Lv, X. Luo, W. J. Lu, Q. L. Pei, G. T. Lin, Y. Y. Han, X. B. Zhu, W. H. Song, Y. P. Sun, Extremely large magnetoresistance in the type-II Weyl semimetal MoTe_2 , *Phys. Rev. B* 94 (2016) 235154.
- [45] N. Wakeham, E. D. Bauer, M. Neupane, F. Ronning, Large magnetoresistance in the antiferromagnetic semimetal NdSb , *Phys. Rev. B* 93 (2016) 205152.

Table 1: Physical parameters of the τ , κ , δ , and α orbits of GaB₄ estimated based on the de Haas-van Alphen (dHvA) oscillations: oscillation frequency F , area of the Fermi surface A_F , Fermi wave vector k_F , cyclotron effective mass m^* , Dingle temperature T_D , scattering time τ , electronic mobility μ , and phase factor $2\pi\Gamma$.

| | τ | κ | δ | α |
|---|--------|----------|----------|----------|
| F (T) | 8.2 | 113 | 126 | 176 |
| A_F (10^{-5} \AA^{-2}) | 78.23 | 1078 | 1202 | 1679 |
| k_F (10^{-3} \AA^{-1}) | 4.99 | 18.52 | 19.56 | 23.12 |
| m^* (m_e) | 0.07 | 0.217 | 0.188 | 0.199 |
| T_D (K) | 0.49 | 6.27 | 7.24 | 3.05 |
| τ (10^{-12} s) | 2.48 | 0.19 | 0.17 | 0.39 |
| μ ($\text{cm}^2 \text{ V}^{-1} \text{ s}^{-1}$) | 56756 | 1402 | 1448 | 3139 |
| $2\pi\Gamma$ (π) | 1.33 | 0.88 | 0.88 | 1.75 |

Table 2: Hall carrier density (Hall mobility) of two electronic bands of n_{e1} (μ_{e1}) and n_{e2} (μ_{e2}) and one hole band n_h (μ_h) at temperatures of $T = 2, 3, 5,$ and 7 K.

| | 2 K | 3 K | 5 K | 7 K |
|--|-------|-------|------|------|
| n_{e1} ($\times 10^{20} \text{ cm}^{-3}$) | 1.17 | 1.73 | 0.82 | 1.17 |
| μ_{e1} ($\text{cm}^2 \text{ V}^{-1} \text{ s}^{-2}$) | 12019 | 17775 | 5788 | 3750 |
| n_{e2} ($\times 10^{17} \text{ cm}^{-3}$) | 5.35 | 6.79 | 2.94 | 5.03 |
| μ_{e2} ($\text{cm}^2 \text{ V}^{-1} \text{ s}^{-2}$) | 3796 | 4559 | 3888 | 6321 |
| n_h ($\times 10^{20} \text{ cm}^{-3}$) | 1.17 | 1.73 | 0.85 | 1.22 |
| μ_h ($\text{cm}^2 \text{ V}^{-1} \text{ s}^{-2}$) | 11550 | 16762 | 5554 | 3645 |

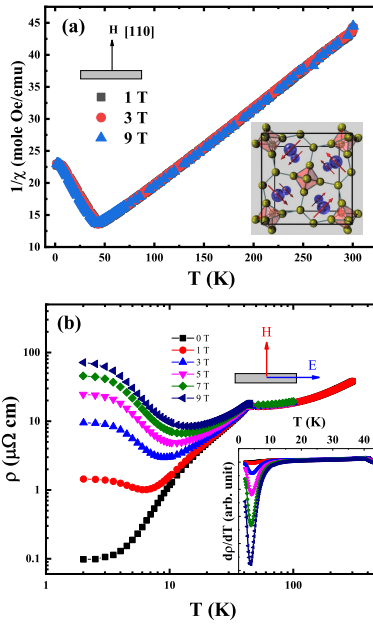


Figure 1: (a) Temperature-dependent inverse magnetic susceptibility $1/\chi$ for applying magnetic fields along the $[110]$ direction. The inset shows the crystal structure and magnetic spin directions of Gd ions in GdB_4 with a non-collinear magnetic structure. (b) Temperature-dependent electrical resistivity for various magnetic fields. A magnetic field is applied along the $[110]$ direction perpendicular to the samples and electric field direction (upper right inset). The lower right inset is the temperature derivative of electrical resistivity $d\rho/dT$ at low temperatures ($T \leq 45$ K).

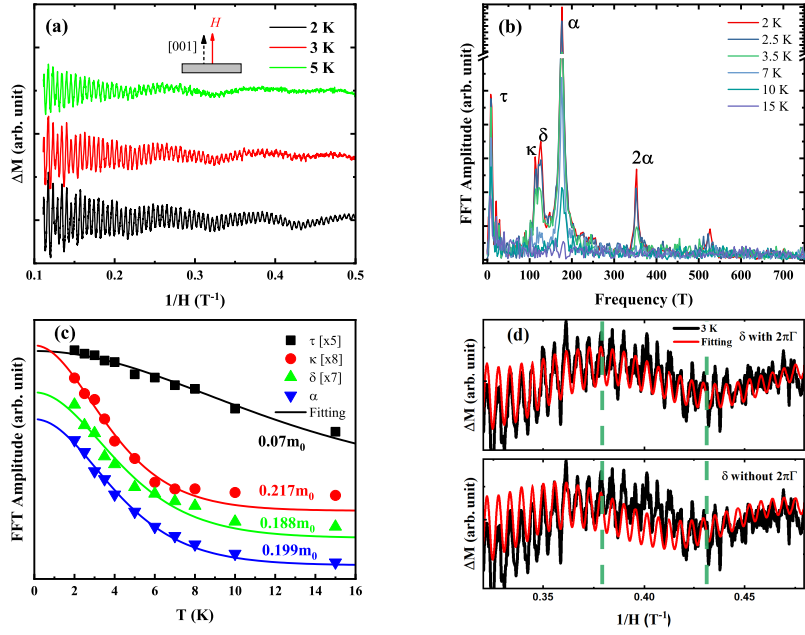


Figure 2: Isothermal de Haas-van Alphen (dHvA) oscillations along the [001] direction. (a) Amplitudes of dHvA oscillations as a function of the inverse magnetic field $1/B$ for isothermal temperatures of 2 K, 3 K, and 5 K. (b) Fast Fourier Transformation (FFT) of the dHvA oscillations where the peaks are assigned as four independent orbits of τ , κ , δ , and α for various temperatures. (c) Temperature-dependent FFT amplitudes of the dHvA oscillations for different orbits (symbols) and fitted curves based on temperature-damping (lines, see text). (d) The dHvA oscillation at 3 K (black line) and its theoretical fitting to the Lifshitz-Kosheovich (LK) formula (red line). The upper (lower) panel depicts the LK formula fitting with (without) $2\pi\Gamma$.

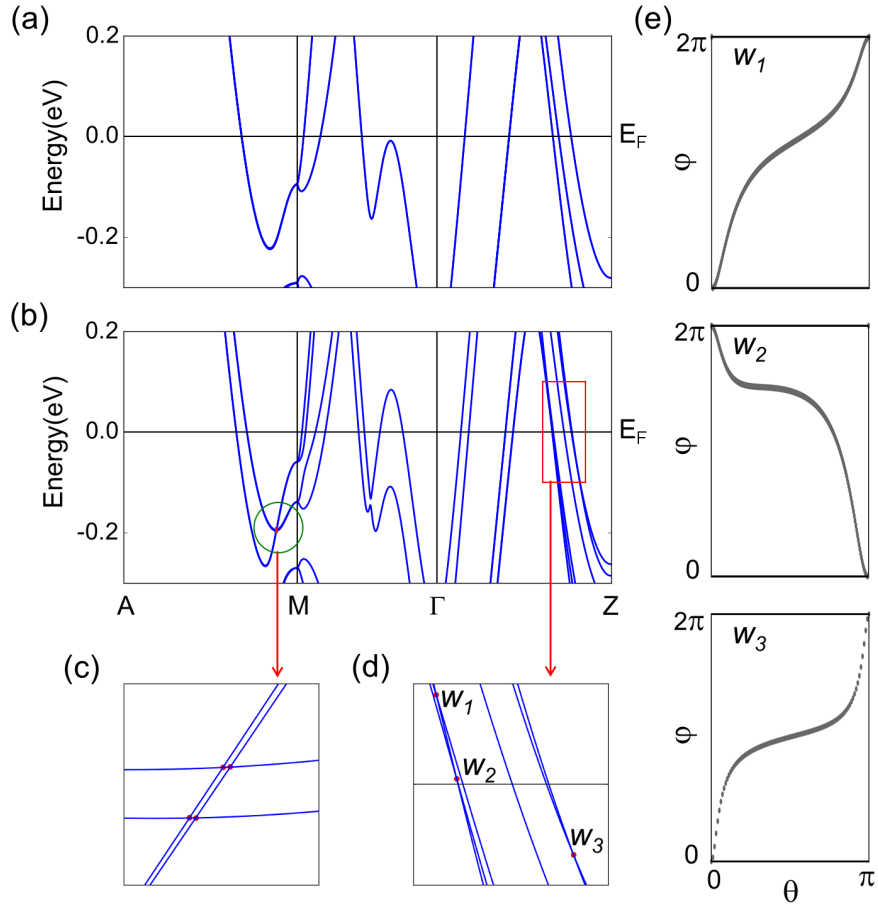


Figure 3: Energy band structure of GdB₄ and Berry's curvature. (a) Electronic energy band structure with a non-collinear spin structure along the A-M- Γ -Z lines. (b) Electronic band structure when applying the magnetic field along the [001] direction. In this case, we assume that the non-collinear spins are slightly tilted along the magnetic field direction. (c, d) Expanded plot near the band crossing points of A-M (green circle) and Γ -Z lines (red square). (e) Wannier charge flow at the Weyl points of WP1, WP2, and WP3, along the Γ -Z line.

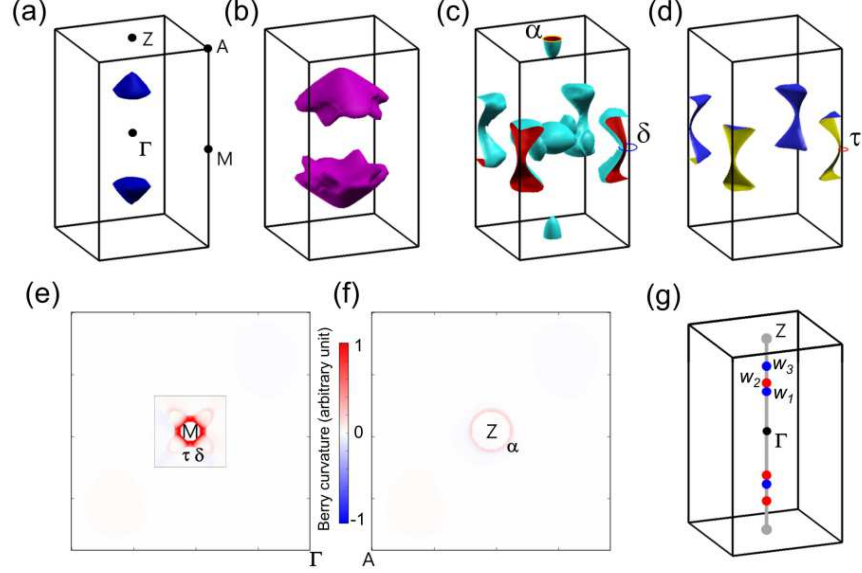


Figure 4: (a-d) Fermi surfaces of GdB_4 . For clarity, we separated each Fermi surface. Integrated Berry curvature near the M-point (τ and δ orbits) (e) and Z-point (α orbit) (f). Weyl points of W_1 , W_2 , and W_3 [the same band points in Fig. 3(d)] along the Γ -Z line.

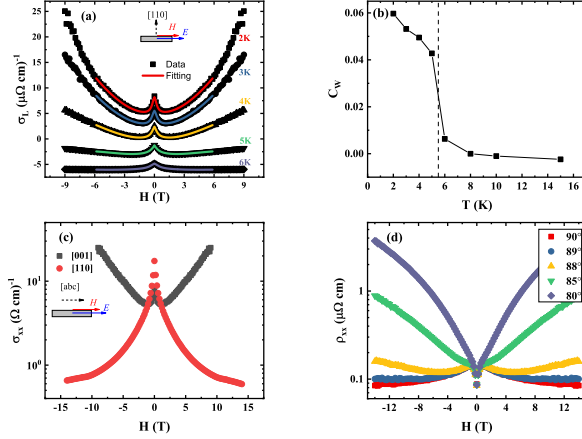


Figure 5: Analysis of negative longitudinal magnetoconductivity in terms of chiral anomaly. (a) Isothermal longitudinal magnetoconductivity $\sigma_L(B)$ at low temperatures (symbols) and theoretical fitting based on the Boltzmann transport equation (lines). (b) Temperature-dependent correction factor C_W showing a sudden jump near 6 K (see text). (c) Longitudinal magnetoconductivity $L(B)$ for applying magnetic fields along the $[110]$ (grey square) and $[001]$ (red circle) directions. (d) Magneto-resistivity at different angles between the directions of the magnetic field and electric field at 2 K. The magnetic field direction is rotated from the $[110]$ direction (0°) to $[001]$ (90°) with the angle from $[110]$.

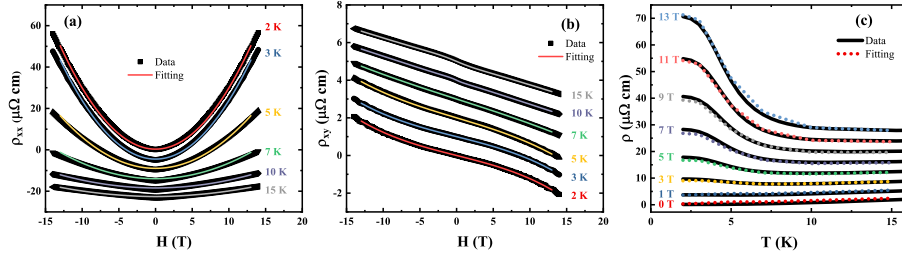


Figure 6: Analysis of the magnetoresistance, Hall resistivity, and temperature-dependent electrical resistivity based on the three-carrier model. (a) Isothermal transverse magnetoresistance $\rho_{xx}(B)$ and (b) Hall resistivity $\rho_{xy}(B)$ at various temperatures with respect to the magnetic field H . The symbols are experimental results and the lines are the fitted results in terms of the three-carrier model (two electrons and one hole as charge carriers). (c) Temperature-dependent electrical resistivity $\rho(T)$ and their simulation curves calculated using the obtained carrier density and mobility from the three-carrier model.